Title

Helium superfluidity. Shapes and vorticities of superfluid helium nanodroplets.

Journal

Science (New York, N.Y.), 345(6199)

ISSN

0036-8075

Authors

Gomez, Luis F

Ferguson, Ken R

Cryan, James P

et al.

Publication Date

2014-08-01

DOI

10.1126/science.1252395

Peer reviewed

25. H. F. Hofmann, K. Kojima, S. Takeuchi, K. Sasaki, . *J. Opt. B* **5**, 218–221 (2003).
26. D. Witthaut, A. S. Sørensen, *New J. Phys.* **12**, 043052 (2010).
27. S. Rosenblum, S. Parkins, B. Dayan, *Phys. Rev. A* **84**, 033854 (2011).
28. J. Gea-Banacloche, W. Wilson, *Phys. Rev. A* **88**, 033832 (2013).
29. H. J. Carmichael, *Phys. Rev. Lett.* **70**, 2273–2276 (1993).
30. Materials and methods are available as supplementary materials on *Science* Online.
31. C. Junge, D. O'Shea, J. Volz, A. Rauschenbeutel, *Phys. Rev. Lett.* **110**, 213604 (2013).
32. We also performed the opposite experiment, in which the control pulses were always σ^-, and the target pulse was half of the times σ^+ and half of the times σ^-. The obtained results were completely consistent with the ones presented here.

ACKNOWLEDGMENTS

Support from the Israeli Science Foundation, the Joseph and Celia Reskin Career Development Chair in Physics, and the Crown Photonics Center is acknowledged. This research was made possible in part by the historic generosity of the Harold Perlman family.

SUPPLEMENTARY MATERIALS

www.sciencemag.org/content/345/6199/903/suppl/DC1
Materials and Methods
Supplementary Text
Figs. S1 to S3
References (*33*, *34*)

11 April 2014; accepted 26 June 2014
Published online 10 July 2014;
10.1126/science.1254699

HELIUM SUPERFLUIDITY

Shapes and vorticities of superfluid helium nanodroplets

Luis F. Gomez,[1]* Ken R. Ferguson,[2] James P. Cryan,[3] Camila Bacellar,[3,4] Rico Mayro P. Tanyag,[1] Curtis Jones,[1] Sebastian Schorb,[2] Denis Anielski,[5,6] Ali Belkacem,[3] Charles Bernando,[7] Rebecca Boll,[5,6,8] John Bozek,[2] Sebastian Carron,[2] Gang Chen,[9]† Tjark Delmas,[10] Lars Englert,[11] Sascha W. Epp,[5,6] Benjamin Erk,[5,6,8] Lutz Foucar,[6,12] Robert Hartmann,[13] Alexander Hexemer,[9] Martin Huth,[13] Justin Kwok,[14] Stephen R. Leone,[3,4,15] Jonathan H. S. Ma,[3,16] Filipe R. N. C. Maia,[17]‡ Erik Malmerberg,[18,19] Stefano Marchesini,[9,20] Daniel M. Neumark,[3,4] Billy Poon,[18] James Prell,[4] Daniel Rolles,[6,8,12] Benedikt Rudek,[5,6]§ Artem Rudenko,[5,6,21] Martin Seifrid,[1] Katrin R. Siefermann,[3]‖ Felix P. Sturm,[3] Michele Swiggers,[2] Joachim Ullrich,[5,6]§ Fabian Weise,[3]¶ Petrus Zwart,[18] Christoph Bostedt,[2,22]# Oliver Gessner,[3]# Andrey F. Vilesov[1,7]#

Helium nanodroplets are considered ideal model systems to explore quantum hydrodynamics in self-contained, isolated superfluids. However, exploring the dynamic properties of individual droplets is experimentally challenging. In this work, we used single-shot femtosecond x-ray coherent diffractive imaging to investigate the rotation of single, isolated superfluid helium-4 droplets containing ~10^8 to 10^{11} atoms. The formation of quantum vortex lattices inside the droplets is confirmed by observing characteristic Bragg patterns from xenon clusters trapped in the vortex cores. The vortex densities are up to five orders of magnitude larger than those observed in bulk liquid helium. The droplets exhibit large centrifugal deformations but retain axially symmetric shapes at angular velocities well beyond the stability range of viscous classical droplets.

The discoveries of superconductors, superfluids, and Bose-Einstein condensates (BECs) (*1*, *2*) reveal that a large number of particles can occupy a single quantum state that extends across macroscopic length scales. A notable example is superfluid ^{4}He (*3*–*6*): It lacks any viscosity below a critical temperature of T_λ = 2.17 K, and its motion is described by a single wave function (*1*, *2*, *5*–*7*). Isolated He nanodroplets were employed to study the onset of superfluidity through the observation of frictionless, quantized rotation of embedded molecules surrounded with varying numbers of ^{4}He atoms (*8*). However, the unambiguous demonstration of a quantum mechanical state of motion of an entire helium nanodroplet remains challenging.

In a finite droplet, any manifestation of liquid flow must involve rotational motion, which, in a superfluid, embodies itself in quantum vortices (*6*, *7*). Indeed, the formation of regular arrays of parallel vortices was detected in a rotating bucket filled with superfluid He (*9*, *10*). However, surprisingly little is known about quantum rotation in superfluid droplets. Calculations predict that vortices may exist in ^{4}He droplets as small as a few nanometers in diameter (*11*–*13*), but experimental studies of this elusive phenomenon remain challenging (*14*). Recently, traces of vortices were detected in He droplets ~1 μm in diameter (*15*). However, these exploratory experiments did not provide detailed hydrodynamic properties of the spinning droplets, such as their shapes or the spatial arrangements of the vortices they contain. In this work, we studied the rotation of single, isolated superfluid He nanodroplets via coherent scattering of x-rays from a free-electron laser (FEL) (*16*–*18*). Figure 1 illustrates the experiment, in which ^{4}He droplets with radii R = 100 to 1000 nm [number of He atoms (N_{He}) = 10^8 to 10^{11}] were produced upon fragmentation of liquid helium expanding into a vacuum (*15*, *19*, *20*) [see section S1 of (*21*)]. After a time of flight of 3.8 ms across a distance of 640 mm from the nozzle, the droplets traversed the focus of the FEL beam [photon energy = 1.5 keV, wavelength λ = 0.827 nm]. Diffraction images were recorded with a pn-junction charge-coupled device detector placed ≈565 mm behind the interaction volume. Each image originates from a single droplet irradiated by a single FEL shot. The low-density core of ^{4}He vortices is ≈0.2 nm in diameter (*7*), which does not provide sufficient contrast for direct detection by x-ray scattering. Therefore, the droplets are doped with Xe atoms ($N_{Xe} \approx 10^{-3} N_{He}$), which cluster along the vortex cores (*10*, *15*) and act as a contrast agent.

Diffraction images of individual neat helium droplets are shown in Fig. 2, A to C. The circular and elliptical diffraction contours in Fig. 2, A and B, are consistent with diffraction from spheroidal droplets with a symmetry half-axis a and two equal perpendicular half-axes b (fig. S2). The aspect ratio AR = (long half-axis)/(short half-axis)

[1]Department of Chemistry, University of Southern California (USC), Los Angeles, CA 90089, USA. [2]Linac Coherent Light Source (LCLS), SLAC National Accelerator Laboratory, 2575 Sand Hill Road, Menlo Park, CA 94025, USA. [3]Ultrafast X-ray Science Laboratory, Chemical Sciences Division, Lawrence Berkeley National Laboratory (LBNL), Berkeley, CA 94720, USA. [4]Department of Chemistry, University of California Berkeley, Berkeley, CA 94720, USA. [5]Max-Planck-Institut für Kernphysik, Saupfercheckweg 1, 69117 Heidelberg, Germany. [6]Max Planck Advanced Study Group at the Center for Free-Electron Laser Science (CFEL), Notkestraße 85, 22607 Hamburg, Germany. [7]Department of Physics and Astronomy, USC, Los Angeles, CA 90089, USA. [8]Deutsches Elektronen-Synchrotron (DESY), Notkestraße 85, 22607 Hamburg, Germany. [9]Advanced Light Source, LBNL, Berkeley, CA 94720, USA. [10]CFEL, DESY, Notkestraße 85, 22607 Hamburg, Germany. [11]Max-Planck-Institut für Extraterrestrische Physik, Giessenbachstraße, 85741 Garching, Germany. [12]Max-Planck-Institut für Medizinische Forschung, Jahnstrasse 29, 69120 Heidelberg, Germany. [13]PNSensor GmbH, Otto-Hahn-Ring 6, 81739 München, Germany. [14]Mork Family Department of Chemical Engineering and Materials Science, USC, Los Angeles, CA 90089, USA. [15]Department of Physics, University of California Berkeley, Berkeley, CA 94720, USA. [16]Department of Physics, The Chinese University of Hong Kong, Hong Kong, China. [17]National Energy Research Scientific Computing Center, LBNL, Berkeley, CA 94720, USA. [18]Physical Biosciences Division, LBNL, Berkeley, CA 94720, USA. [19]Department of Plant and Microbial Biology, University of California Berkeley, Berkeley, CA 94720, USA. [20]Department of Physics, University of California Davis, Davis, CA 95616, USA. [21]James R. Macdonald Laboratory, Department of Physics, Kansas State University, Manhattan, KS 66506, USA. [22]PULSE Institute, Stanford University and SLAC National Accelerator Laboratory, 2575 Sand Hill Road, Menlo Park, CA 94025, USA.
*Present address: New Focus, 3635 Peterson Way, Santa Clara, CA 95054, USA. †Present address: Shanghai Synchrotron Radiation Facility, Shanghai Institute of Applied Physics, Chinese Academy of Sciences, Shanghai 201204, China. ‡Present address: Department of Cell and Molecular Biology, Uppsala University, Husargatan 3, Uppsala 75124, Sweden. §Present address: Physikalisch-Technische Bundesanstalt, Bundesallee 100, D-38116 Braunschweig, Germany. ||Present address: Leibniz Institute of Surface Modification (IOM), Permoserstraße 15, 04318 Leipzig, Germany. ¶Present address: Berliner Glas KGaA Herbert Kubatz GmbH, Waldkraiburger Straße 5, 12347 Berlin, Germany.
#Corresponding author. E-mail: bostedt@slac.stanford.edu (C.B.); ogessner@lbl.gov (O.G.); vilesov@usc.edu (A.F.V.)

≥ 1 of the diffraction contours quantifies the distortion of the droplets from a spherical shape (AR = 1). Each diffraction image reflects the projection of a single droplet's density profile onto the detector plane; the longer axis in the diffraction pattern corresponds to the shorter droplet axis and vice versa. Because the a axis subtends an arbitrary angle with the x-ray beam, only the b axis and an upper boundary $a \leq b/AR$ can be deduced from each image. The pattern in Fig. 2A originates from either a spherical droplet with $R = a = b = 298 \pm 5$ nm or a spheroidal droplet with $b = R$ and its a axis aligned parallel to the x-ray beam. The diffraction pattern in Fig. 2B corresponds to a spheroid with $b = 284 \pm 5$ nm and $a \leq 0.87b = 247 \pm 5$ nm [section S2 of (*21*)].

Approximately ~1% of the diffraction images cannot be described by ellipses and exhibit very high aspect ratios of $1.7 < AR < 2.3$, such as AR = 1.92 in Fig. 2C. Figure 2D shows the outline of the corresponding droplet, which was obtained by inverse Fourier transform (IFT) of Fig. 2C [section S3 of (*21*)]. The droplet is wheel-shaped with two nearly parallel surfaces and half-axes $a = 220 \pm 15$ nm and $b = 422 \pm 10$ nm. The intense diagonal streak in Fig. 2C indicates that the droplet was imaged edge-on within ± 5° [see section S3 of (*21*)]. Thus, values for both a and b can be determined.

Our measurements reveal that, on average, ~40% of He droplets [section S5 of (*21*)] in the beam are not spherical, as was previously assumed (*20*), but are better represented by spheroids or wheel shapes. In general, a droplet may acquire a nonspherical shape due to rotational or vibrational excitation. However, our estimates show that vibrational shape oscillations should decay before the interaction point [section S6 of (*21*)]. Therefore, the elliptical and streaked diffraction patterns are ascribed to oblate rotating droplets. The droplet rotation probably originates from inhomogeneous flow of helium through the nozzle during the expansion (*15*).

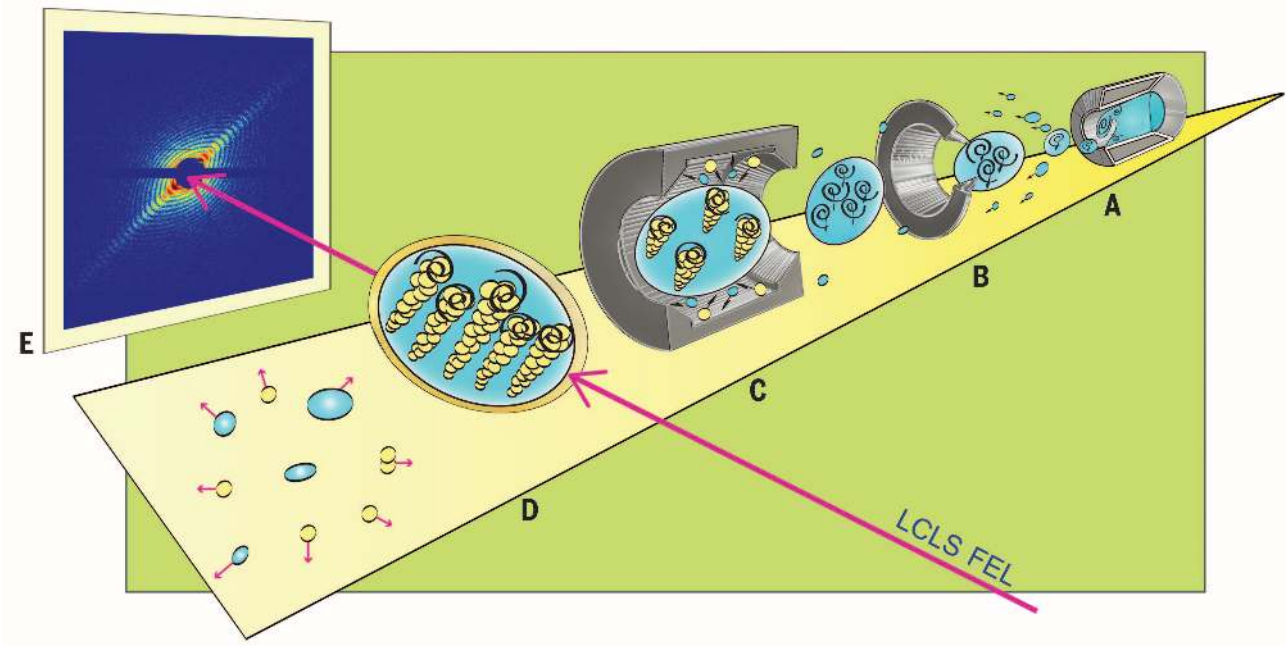

Fig. 1. Experimental setup. (**A**) Rotating droplets are produced by expanding He fluid into a vacuum through a 5-μm nozzle at a temperature of $T_0 \approx 5$ K and a backing pressure $P_0 = 20$ bar. (**B**) Quantum vortices form upon evaporative cooling of rotating droplets to below T_λ. (**C**) Droplets are doped with Xe atoms in a cell filled with Xe gas. (**D** and **E**) X-ray diffraction images of single droplets are recorded using single FEL light pulses.

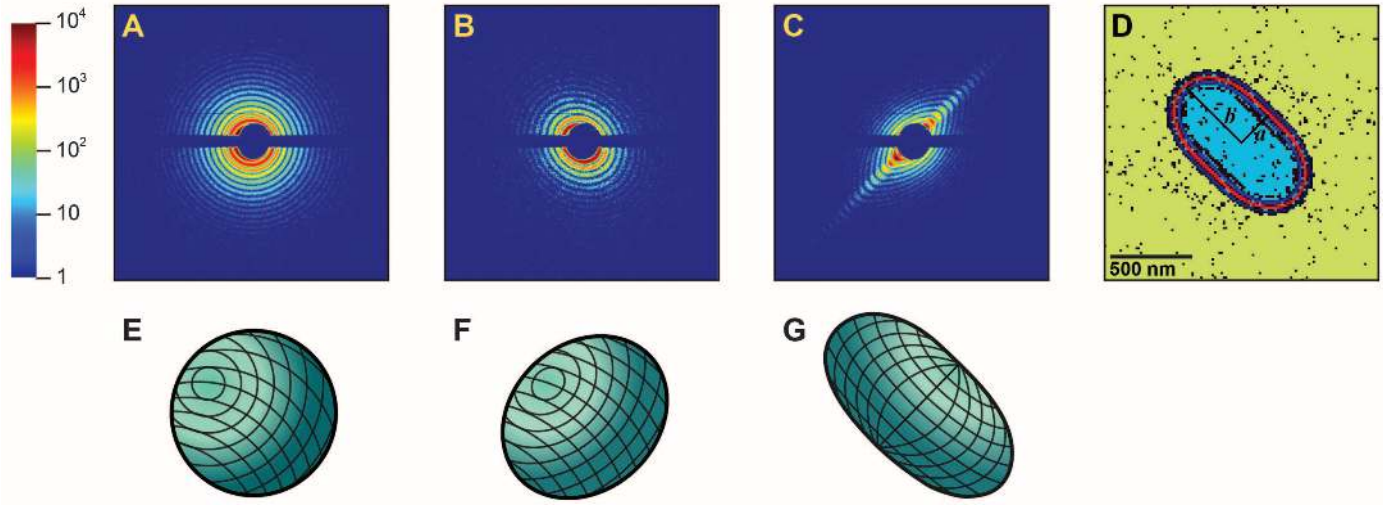

Fig. 2. X-ray diffraction images of neat He droplets. Images in (**A**) to (**C**) represent circular, elliptical, and streaked patterns, respectively, displayed in a logarithmic color scale. (**D**) Image showing a droplet outline reconstructed from the diffraction pattern in (C) by IFT. Note that the droplet itself is not hollow but filled. (**E** to **G**) 3D representations of the droplet shapes in (A) to (C) have been placed below the corresponding images.

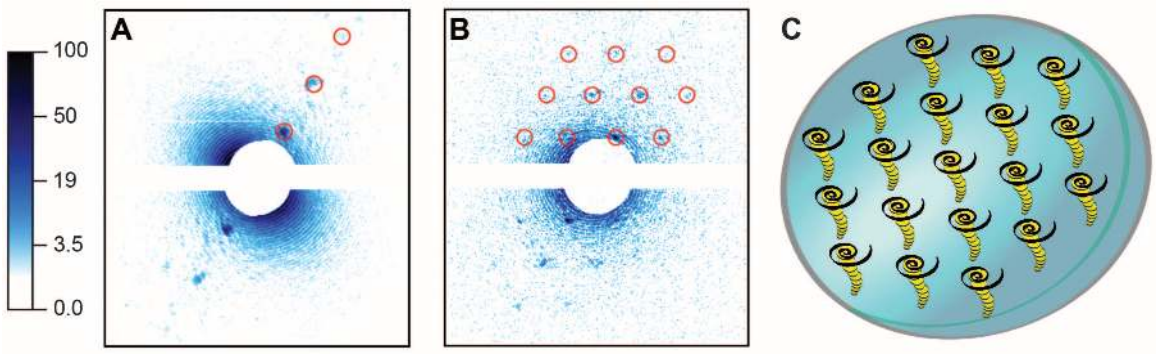

Fig. 3. He droplets doped with Xe atoms. (**A** and **B**) X-ray diffraction images of doped droplets, displayed in a logarithmic intensity scale. (**C**) Droplet and embedded Xe clusters. Images in (A) and (B) correspond to tilted and parallel alignments of the vortex axes with respect to the incident x-ray beam, respectively.

The shapes adopted by the rotating quantum droplets display similarities and pointed differences when compared with their classical counterparts. A classical droplet, rotating as a rigid body, can be described by the reduced angular velocity

$$\Omega = \sqrt{\frac{3\rho V}{32\pi\sigma}}\,\omega \qquad (1)$$

which defines the droplet's aspect ratio (*22*, *23*). Here, ρ is the density, σ is the surface tension, V is the volume of the droplet, and ω is its angular velocity. No droplet is stable beyond the disintegration limit of $\Omega_{MAX} = 0.75$. At small Ω, a droplet has a spheroidal shape. Beyond $\Omega = 0.56$ ($b/a = 1.50$), viscous classical droplets become unstable and begin to exhibit two-lobed shapes, resembling a peanut that rotates around its short axis. Multilobed droplet shapes emerge at even higher Ω (*22*–*24*). In this work, we observe axially symmetric droplets with aspect ratios as high as $b/a = 2.3$, corresponding to $\Omega = 0.71$ [section S4 of (*21*)], which is considerably higher than the shape instability threshold of classical droplets. No evidence for multilobed shapes was detected. Our results confirm the predicted extended range of stability in rotating quantum liquids (*23*) and indicate that superfluid droplets remain axially symmetric up to rotational speeds close to Ω_{MAX}.

The angular velocities (ω) of rotating droplets can be determined from the degree of centrifugal distortion, quantified by the a and b half-axes [section S4 of (*21*)] (*23*). For the image in Fig. 2C, this analysis leads to $\omega = 1.4 \times 10^7\ s^{-1}$. The rotation of a superfluid may manifest as a lattice of uniformly distributed parallel vortices (*1*, *6*, *7*, *9*) with an area density of

$$n_V = \frac{2\omega M}{h} \qquad (2)$$

Here, M is the mass of the ^{4}He atom, h is Planck's constant, and n_V is the number of vortices per unit area in a plane perpendicular to the axis of rotation (*6*, *7*). For the droplet imaged in Fig. 2C, Eq. 2 predicts a vortex density of $n_V = 2.8 \times 10^{14}\ m^{-2}$ and a total number of vortices of $N_V = \pi b^2 n_V = 160$. Evidently, droplets in the beam are characterized by a substantial degree of rotational excitation and thus should contain large numbers of quantum vortices. The existence of these vortices is confirmed by doping the He droplets with Xe atoms.

Figure 3 shows diffraction images of He droplets doped with Xe atoms. In addition to the characteristic ring patterns from the droplets, many images exhibit Bragg spots that either lie on a line crossing the image center (Fig. 3A) or form an equilateral triangular pattern (Fig. 3B). The Bragg spot separations in Fig. 3 correspond to regularly spaced Xe structures with periods of $d \approx 100$ nm, whereas the ring patterns arise from a droplet with $R \approx 1$ μm. These numbers are consistent with the condensation of Xe atoms along the cores of multiple parallel vortices arranged in a lattice within the superfluid droplet (Fig. 3C). According to this model, both linear and triangular Bragg spot arrangements emerge from ordered lattices with different relative angles between the x-ray beam and the vortex lines. The actual shape of the vortices cannot be determined from the Bragg spots, although the vortices in the arrays are expected to have some curvature as they terminate perpendicular to the droplet's surface. Approximately 5% of the doped droplet images exhibit Bragg spots. Considering that the appearance of Bragg spots depends critically on the relative alignment of the vortex structures and the x-ray beam, which is randomly distributed in these experiments, we estimate that ~50% of droplets contain vortex lattices [section S7 of (*21*)].

The identification of quantum vortices provides direct evidence of the superfluidity of He nanodroplets. The appearance of triangular vortex arrangements agrees with previous observations of triangular arrays of quantum vortices in rarified BECs (*25*, *26*). The diameters of the vortex cores in superfluid He, however, are small compared with the droplet sizes and the vortex length scales, which can lead to extended, three-dimensional (3D) vortex arrangements.

The diffraction pattern in Fig. 3B provides a direct measure of the vortex density, $n_V = 4.5 \times 10^{13}\ m^{-2}$, and the droplet radius, $b = 1100$ nm, corresponding to a total number of vortices $N_V = 170$. The angular velocity of the rotating droplet is $\omega = 2.2 \times 10^6\ s^{-1}$ (Eq. 2). The diffraction rings in Fig. 3B are circular within the experimental resolution (~3%). This observation and, in particular, the emergence of the triangular Bragg pattern, indicate that the droplet was imaged almost exactly along the a axis. From the angular velocity and the equatorial radius b, the aspect ratio and reduced angular velocity of the droplet are estimated to be $AR = 1.34$ and $\Omega = 0.50$, respectively [section S4 of (*21*)]. These values fall well within the axisymmetric shape stability limits for rotating droplets. The vortex density in this droplet is about five orders of magnitude larger than previously observed in rotating bucket experiments with bulk superfluid helium (*9*, *10*). These numbers demonstrate that superfluid He droplets provide access to unexplored regimes of rotational excitation in quantum liquids. It is intriguing that, although observation of the wheel shapes in smaller droplets ($b \approx 300$ to 400 nm) indicates the existence of high vortex densities in the range of $n_V \approx 3 \times 10^{14}\ m^{-2}$, no corresponding Bragg patterns were observed in these droplets [section S7 of (*21*)]. This may indicate that vortices at extremely high densities fail to crystallize and instead form a disordered state with little resemblance to a lattice. Another possibility is the existence of nonequilibrium states, which may be related to quantum turbulence. However, estimates [section S6 of (*21*)] show that turbulence, which accompanies establishment (*27*) or breakdown (*28*) of equilibrium quantum rotation, decays before the interaction point. Hydrodynamic instability of the droplet shape at high angular velocities may also disrupt vortex arrays. The possibility for the formation of nonstationary vortex states in superfluid helium has been discussed (*6*) but has never been confirmed experimentally. In addition, BECs at high ω are predicted to undergo a quantum phase transition into a highly correlated nonsuperfluid state devoid of any vortices (*26*). It would therefore be interesting to explore whether similar concepts apply to rotating He droplets at high ω.

REFERENCES AND NOTES

1. L. Pitaevskii, S. Stringari, *Bose-Einstein Condensation*, J. Birman *et al.*, Eds. (vol. 116 of The International Series of Monographs on Physics, Clarendon Press, Oxford, 2003).
2. D. R. Tilley, J. Tilley, *Superfluidity and Superconductivity* (Institute of Physics Publishing, Bristol, UK, 1990).
3. J. F. Allen, A. D. Misener, *Nature* **141**, 75 (1938).

4. P. Kapitza, *Nature* **141**, 74 (1938).
5. L. D. Landau, *J. Phys. (Moscow)* **5**, 185–204 (1941).
6. R. P. Feynman, in *Progress in Low Temperature Physics*, C. J. Gorter, Ed. (North-Holland, Amsterdam, 1955), vol. 1, pp. 1–53.
7. R. J. Donnelly, *Quantized Vortices in Helium II*, A. M. Goldman, P. V. E. McKlintock, M. Springford, Eds. (vol. 3 of Cambridge Studies in Low Temperature Physics, Cambridge Univ. Press, Cambridge, 1991).
8. S. Grebenev, J. P. Toennies, A. F. Vilesov, *Science* **279**, 2083–2086 (1998).
9. E. J. Yarmchuk, M. J. V. Gordon, R. E. Packard, *Phys. Rev. Lett.* **43**, 214–217 (1979).
10. G. P. Bewley, D. P. Lathrop, K. R. Sreenivasan, *Nature* **441**, 588 (2006).
11. G. H. Bauer, R. J. Donnelly, W. F. Vinen, *J. Low Temp. Phys.* **98**, 47–65 (1995).
12. K. K. Lehmann, R. Schmied, *Phys. Rev. B* **68**, 224520 (2003).
13. M. Barranco *et al.*, *J. Low Temp. Phys.* **142**, 1–81 (2006).
14. M. A. Weilert, D. L. Whitaker, H. J. Maris, G. M. Seidel, *J. Low Temp. Phys.* **106**, 101–131 (1997).
15. L. F. Gomez, E. Loginov, A. F. Vilesov, *Phys. Rev. Lett.* **108**, 155302 (2012).
16. L. Strüder *et al.*, *Nucl. Instrum. Methods A* **614**, 483–496 (2010).
17. C. Bostedt *et al.*, *J. Phys. B* **46**, 164003 (2013).
18. T. Gorkhover *et al.*, *Phys. Rev. Lett.* **108**, 245005 (2012).
19. L. F. Gomez, E. Loginov, R. Sliter, A. F. Vilesov, *J. Chem. Phys.* **135**, 154201 (2011).
20. J. P. Toennies, A. F. Vilesov, *Angew. Chem. Int. Ed.* **43**, 2622–2648 (2004).
21. Materials and methods and supporting analysis of the experimental data are available as supplementary materials on *Science* Online.
22. R. A. Brown, L. E. Scriven, *Proc. R. Soc. London Ser. A* **371**, 331–357 (1980).
23. S. Chandrasekhar, *Proc. R. Soc. London Ser. A* **286**, 1–26 (1965).
24. R. J. A. Hill, L. Eaves, *Phys. Rev. Lett.* **101**, 234501 (2008).
25. J. R. Abo-Shaeer, C. Raman, J. M. Vogels, W. Ketterle, *Science* **292**, 476–479 (2001).
26. A. L. Fetter, *Rev. Mod. Phys.* **81**, 647–691 (2009).
27. A. P. Finne *et al.*, *Nature* **424**, 1022–1025 (2003).
28. P. M. Walmsley, A. I. Golov, H. E. Hall, A. A. Levchenko, W. F. Vinen, *Phys. Rev. Lett.* **99**, 265302 (2007).

ACKNOWLEDGMENTS

This work was supported by NSF grant CHE-1112391 (A.F.V.) at USC; the U.S. Department of Energy (DOE), Office of Basic Energy Sciences (OBES), Chemical Sciences, Geosciences and Biosciences Division through contract no. DE-AC02-05CH11231; and the Max Planck Society by funding the development and operation of the CFEL Advanced Study Group (ASG) Multi-Purpose (CAMP) instrument. Portions of this research were carried out at the LCLS, a national user facility operated by Stanford University on behalf of the U.S. DOE OBES under beam-time grant L549: Imaging of quantum vortices in superfluid helium droplets. S.R.L. and J.P. acknowledge support from the Office of the Secretary of Defense, National Security Science and Engineering Faculty Fellowship. C.B. was partially supported through the PULSE Institute at SLAC National Accelerator Laboratory funded by the U.S. DOE OBES under contract no. DE-AC02-76SF00515. J.K. was supported by the USC Undergraduate Research Associates Program. S.M. was supported by the Center for Applied Mathematics for Energy Research Applications (CAMERA). A.R. was supported by the NSF. M. Seifrid was supported by the USC Dornsife College of Letters, Arts and Sciences Student Opportunities for Academic Research and Summer Undergraduate Research Fund fellowships. K.R.S. was supported by the Alexander von Humboldt Foundation.

SUPPLEMENTARY MATERIALS

www.sciencemag.org/content/345/6199/906/suppl/DC1
Materials and Methods
Supplementary Text
Figs. S1 to S6
References (*29*–*39*)

19 February 2014; accepted 20 June 2014
10.1126/science.1252395

NANOPARTICLE IMAGING

Electron microscopy of gold nanoparticles at atomic resolution

Maia Azubel,[1] Jaakko Koivisto,[2] Sami Malola,[3] David Bushnell,[1] Greg L. Hura,[4] Ai Leen Koh,[5] Hironori Tsunoyama,[6]* Tatsuya Tsukuda,[6]† Mika Pettersson,[2] Hannu Häkkinen,[2,3] Roger D. Kornberg[1]‡

Structure determination of gold nanoparticles (AuNPs) is necessary for understanding their physical and chemical properties, but only one AuNP larger than 1 nanometer in diameter [a 102–gold atom NP (Au_{102}NP)] has been solved to atomic resolution. Whereas the Au_{102}NP structure was determined by x-ray crystallography, other large AuNPs have proved refractory to this approach. Here, we report the structure determination of a Au_{68}NP at atomic resolution by aberration-corrected transmission electron microscopy, performed with the use of a minimal electron dose, an approach that should prove applicable to metal NPs in general. The structure of the Au_{68}NP was supported by small-angle x-ray scattering and by comparison of observed infrared absorption spectra with calculations by density functional theory.

Gold nanoparticles (AuNPs) are of both fundamental and practical interest. Particles on the order of 1 nm in diameter exhibit distinctive physical and chemical properties, with potential applications ranging from quantum electronics to biomedicine (*1*–*3*). The x-ray crystal structure of a 102–gold atom NP (Au_{102}NP), 1.5 nm in diameter, showed the cluster of gold atoms surrounded by 44 thiolate ligands (*4*). This atomic structure had threefold importance: (i) It identified the Au_{102}NP as a molecule, with a precise composition and distinct arrangement of atoms; (ii) it led to the idea of the gold cluster as a "super atom," stabilized by the filling of electron shells; and (iii) it revealed a layer of alternating gold and ligand molecules at the interface with solution (*5*). Subsequent x-ray structures of much smaller organosoluble AuNPs have supported the super-atom idea and have shown a similar gold-thiol surface layer [reviewed in (*6*)]. Structure determination of other water-soluble AuNPs, and of larger NPs in general, has so far been unsuccessful. Although water-soluble AuNPs ranging from 1 to 3 nm in diameter have been crystallized, x-ray diffraction has not extended beyond ~5 Å resolution. Here, we demonstrate the structure determination of a AuNP by a combination of a low-dose approach and aberration-corrected transmission electron microscopy (TEM), and we report an atomic structure with both similarities and notable differences from the Au_{102}NP.

Whereas the thiolate ligand of the Au_{102}NP was *p*-mercaptobenzoic acid (*p*-MBA), we have now performed synthesis with 3-MBA, resulting in a different set of uniform, water-soluble particles. The product of synthesis with a thiol:gold ratio of 2:1 formed a single sharp band upon gel electrophoresis, with a mobility greater than that of the Au_{102}NP, indicative of a smaller size, as confirmed by cryogenic TEM (fig. S1). Electrospray ionization time-of-flight mass spectrometry (MS) revealed four peaks corresponding to various charged forms of a compound of ~18 kD with a gold core of ~14 kD (fig. S2). A stable AuNP with a gold core of similar size was previously reported by Whetten *et al.* (*7*). Because the mass difference between three atoms of gold [m = 591 atomic mass units (amu)] and four molecules of 3-MBA (m = 613 amu) could not be resolved, the MS result was consistent with the possible molecular formulas $[Au_{71}(3\text{-MBA})_{27}]^{n-}$, $[Au_{68}(3\text{-MBA})_{31}]^{n-}$, $[Au_{68}(3\text{-MBA})_{32}]^{n-}$, $[Au_{65}(3\text{-MBA})_{35}]^{n-}$, and $[Au_{62}(3\text{-MBA})_{39}]^{n-}$ (where n is 5, 6, 7, or 8). We could distinguish among these possibilities by thermogravimetric analysis (TGA) and x-ray photoelectron spectroscopy (XPS). TGA gave a weight loss of 24.4% (fig. S3), compared with values of 26.2% expected for $Au_{68}(3\text{-MBA})_{31}$ or 26.8% expected for $Au_{68}(3\text{-MBA})_{32}$, both discrepancies within the error of the method (*8*). By contrast, expected TGA weight loss values of 29.6% for $Au_{65}(3\text{-MBA})_{35}$ and 33.0% for $Au_{62}(3\text{-MBA})_{39}$ represent discrepancies three to five times greater. XPS gave signals corresponding to Au, S, C, and O (fig. S4), and the peak intensities corresponding to Au_{4f} and S_{2p} were integrated to establish the ratio between Au and organic material. The difference between the values of 65.5% Au and 34.5% S measured and those of 68.7% Au and 31.3% S expected for $Au_{68}(3\text{-MBA})_{31}$ or 68.0% Au and 32.0% S expected for $Au_{68}(3\text{-MBA})_{32}$ were again within the error of the method (*8*). Values of 72.4% Au and 27.6% S expected for $Au_{71}(3\text{-MBA})_{27}$

[1]Department of Structural Biology, Stanford University School of Medicine, Stanford, CA 94305, USA. [2]Department of Chemistry, Nanoscience Center, University of Jyväskylä, FI-40014 Jyväskylä, Finland. [3]Department of Physics, Nanoscience Center, University of Jyväskylä, FI-40014 Jyväskylä, Finland. [4]Physical Bioscience Division, Lawrence Berkeley National Lab, Berkeley, CA 94720, USA. [5]Stanford Nanocharacterization Laboratory, Stanford University, Stanford, CA 94305, USA. [6]Catalysis Research Center, Hokkaido University, Sapporo, Japan.
*Present address: Department of Chemistry, Faculty of Science and Technology, Keio University, Yokohama 223-8522, Japan.
†Present address: Department of Chemistry, School of Science, The University of Tokyo, Tokyo 113-0033, Japan. **‡Corresponding author. E-mail: kornberg@stanford.edu**